JOURNAL OF GEOPHYSICAL RESEARCH, VOL. 97, NO. C8, PAGES 12,671–12,682, AUGUST 15, 1992

Validation and Assimilation of Seasat Altimeter Wave Heights Using the WAM Wave Model

EVA BAUER,[1] SUSANNE HASSELMANN, AND KLAUS HASSELMANN

Max-Planck-Institut für Meteorologie, Hamburg, Germany

HANS C. GRABER[2]

Woods Hole Oceanographic Institution, Woods Hole, Massachusetts

The mutual consistency of the Seasat global data sets of scatterometer winds and altimeter wave heights is investigated for the complete Seasat period using the third-generation wave model WAM. The wave model was driven by surface (1000 hPa) wind and surface stress fields constructed by the Goddard Laboratory for Atmospheres (GLA) by assimilation of the scatterometer winds in an atmospheric model. For the 10-day period September 7–17 the intercomparison was extended to two further scatterometer wind fields: a 1000-hPa assimilated wind field from the European Centre for Medium-Range Weather Forecasts and a subjectively analyzed 19.5-m-height surface wind field from the Jet Propulsion Laboratory. On the global average, the modeled and observed wave heights agree reasonably well. Regional differences, however, can be large and sometimes exceed 40%. The errors are attributed mainly to deficiencies in the forcing wind fields. Low wind speeds are found to be overestimated and high wind speeds underestimated by the Seasat scatterometer algorithm. The friction velocities of the GLA model are found to be significantly underestimated in the high-wind belt of the southern hemisphere. The analysis demonstrates the diagnostic advantages of applying a wave model for the quality assessment of satellite wind and wave data. A preliminary wave data assimilation scheme is presented in which the wave field is updated without changing the forcing wind field. A considerable improvement of the computed wave field is achieved, particularly in regions in which the wave energy is dominated by swell. However, a more general assimilation scheme including modifications of the wind field is needed to upgrade wind sea forecasts.

1. INTRODUCTION

The goal of this study is to investigate the extent to which satellite-derived wind and wave data can be cross validated and assimilated using a state-of-the-art third generation wave model. The principal motivation of the study is the anticipated launch in this decade of a series of ocean satellites (ERS-1, 2, TOPEX-POSEIDON, SPINSAT, ADEOS, RADARSAT, etc.) which will provide global surface wind and sea state data from a variety of all weather microwave sensors. Scatterometers measure surface wind speeds and directions, altimeters provide accurate measurements of the significant wave height and an estimate of the wind speed, and synthetic aperture radars (SARs) yield valuable directional information on the two-dimensional wave spectrum. Ultimately, the voluminous data streams from these sensors will need to be continually analyzed, cross validated, assimilated and applied for operational forecasting in a comprehensive end-to-end system encompassing both the sensor algorithms and high-resolution models. On the input side, sensor algorithms need to be incorporated within the complete system, since most active ocean microwave sensors respond to both wind and sea state and can be effectively deconvoluted only with the aid of algorithms using first-guess data from models. At the output end, sophisticated atmospheric circulation and global wave models are needed to combine the ocean satellite data with conventional data in an optimal, dynamically consistent, space-time-gridded reconstruction of the global wind and wave fields and, of course, to provide forecasts [*K. Hasselmann*, 1985]. Our study may be viewed as a contribution toward the development of such a comprehensive data-processing system.

Seasat, despite its short lifetime, provided an ideal data set to test some of the elements of such an integrated system, since its payload already included most of the active microwave instruments foreseen for future ocean observing missions. The present paper is believed to be the first attempt to intercompare the complete Seasat wind and wave data set (except for the SAR data, which will be considered in a separate paper) in a single combined analysis. An extension of this intercomparison study to ocean buoy data is given by H. C. Graber et al. (manuscript in preparation, 1992).

The algorithms used to derive wind and wave data from the Seasat scatterometer, altimeter, and SAR have been the subject of extensive studies. The backscattered signals of these active microwave surface sensing instruments generally depend on the near-surface wind, the sea state, and also the planetary boundary layer of the atmosphere and the ocean mixed layer [*Brown*, 1986].

Scatterometers measure the ocean radar cross section at medium incidence angles for which the backscattered return is largely governed by Bragg scattering from surface wave ripples. The empirically established dependence of the backscatter cross-section on wind speed and wind direction relative to the scatterometer look direction was used in Seasat to infer surface wind velocities from measurements in

[1]Now at Institut für Meereskunde, University of Hamburg, Hamburg, Germany.

[2]Now at Applied Marine Physics, Rosenstiel School for Marine and Atmospheric Science, University of Miami, Miami, Florida.

Paper number 92JC01056.
0148-0227/92/92JC-01056$05.00

two look directions [*Schroeder et al.*, 1982; *Wentz et al.*, 1986; *Hoffman*, 1982, 1984]. Seasat scatterometer winds have been successfully validated in a number of comparisons with sea truth observations [e.g., *Brown*, 1983; *Duffy and Atlas*, 1986; *Freilich and Chelton*, 1986; *Woiceshyn et al.*, 1986]. Nevertheless, our analysis indicates some deficiencies in the Seasat scatterometer algorithm, in support of similar findings by *Wentz et al.* [1986], *Liu* [1984], and *Anderson et al.* [1987].

Altimeter wind speeds are inferred from the variance of the sea surface slope, which is inversely proportional to the reflected energy for nadir-looking radars [*Mognard et al.*, 1986]. Altimeter winds are generally less accurate than scatterometer wind speeds. *Chelton and McCabe* [1985] and *K. Hasselmann et al.* [1988], for example, found that altimeter wind speeds were significantly lower than scatterometer winds for velocities exceeding 10 m s^{-1} (see also Graber et al. (manuscript in preparation, 1992)).

The flattening of the altimeter return pulse shape yields a rather accurate measure of the significant wave height, with errors typically in the 10% range. Comparisons of the Seasat altimeter wave heights with buoy data along the east, west, and gulf coasts of the United States yielded a mean difference of 0.07 m and a standard deviation of 0.29 m over a wave height range of 0.5 to 5.0 m [*Fedor and Brown*, 1982]. A similar comparison with North Atlantic ship reports for higher sea states (up to 8 m wave height) yielded a bias of less than 0.2 m and a standard deviation of about 0.8 m [*Queffeulou*, 1983].

Information on the two-dimensional ocean wave directional spectrum can be extracted from SAR image spectra. However, the theory of the SAR imaging of ocean waves, including the significant nonlinear distortions induced by the orbital wave motions [cf. *Alpers and Rufenach*, 1979; *Alpers*, 1983; *K. Hasselmann et al.*, 1985, 1991], and the inversion of the imaging computations required to infer ocean wave spectra from observed SAR spectra [*K. Hasselmann and S. Hasselmann*, 1991], are rather complex and will not be considered in this study. SAR images were furthermore obtained only intermittently during the limited Seasat lifetime [see *K. Hasselmann et al.*, 1988], so that these data could not be readily included in the present global analysis of the complete Seasat wind and wave data set extending over the entire Seasat period.

The mutual consistency of the Seasat wind and wave data sets are tested in this study by comparing hindcast wave heights, using the WAM third-generation wave model [*S. Hasselmann et al.*, 1988], and scatterometer-derived wind fields against observed altimeter wave heights. Global near-surface wind and wind stress fields were kindly provided for the total Seasat period (July 7 to October 10, 1978) by the Goddard Laboratory for Atmospheres (GLA) [*Atlas et al.*, 1987]. In addition, the European Centre for Medium-Range Weather Forecasts (ECMWF) [*Anderson et al.*, 1987], and the Jet Propulsion Laboratory (JPL) [*Woiceshyn et al.*, 1986] provided wind velocity fields for shorter periods in September 1978. As the significant wave height for a fully developed wave spectrum [*Pierson and Moskowitz*, 1964] is proportional to the square of the wind velocity, the modeled wave heights can be expected to provide a rather sensitive indicator of errors in the wind and stress fields. This is indeed confirmed in our hindcast simulations.

The sensitive dependence of waves to the wind implies that in a combined wind and wave data assimilation scheme, wave observations should have a significant impact on the wind field analysis. However, the rigorous derivation of wind field corrections from wave data is a nontrivial exercise involving the inversion of the wave model propagation operator (cf. K. Hasselmann et al., manuscript in preparation, 1992) or, equivalently, the integration of an adjoint wave model [e.g., *de Valk and Calkoen*, 1989]. In the present paper we therefore consider only a simplified wave data assimilation system in which the observed altimeter wave heights are introduced into the wave model without modifying the wind field. As expected, the method is most efficient in regions in which the sea consists largely of swell, while in regions dominated by wind seas the corrected wave field relaxes back rather rapidly to the original sea state generated by the unmodified wind field. Alternative assimilation schemes in which the wind field is also changed, but using still a relatively simple ad hoc approach, are described by *Thomas* [1988] and *Janssen et al.* [1989].

The paper is structured as follows. The third-generation wave model used to compute the global wave fields and examples of the hindcast wave height fields are described in section 2. The method of quality control and the global distributions of the altimeter wave heights are presented together with a statistical comparison of the observed and computed wave heights in section 3. In section 4 the differences between the observed and hindcast wave height fields are analyzed and attributed to deficiencies in the analyzed wind and stress fields. Section 5 describes the impact of assimilating the altimeter wave data into the wave model. Section 6, finally, lists the principal conclusions drawn from our study.

2. The WAM Wave Model and Examples of Global Wave Hindcasts

The third-generation wave model WAM used in this study has been extensively tested in a number of hindcast studies [e.g., *S. Hasselmann et al.*, 1988; *Brüning et al.*, 1988; *Romeiser*, 1990]. An essential characteristic of a third-generation wave model is that the spectral energy distribution is computed by direct integration of the basic spectral energy balance equation

$$\frac{\partial F}{\partial t} + \frac{1}{\cos\phi}\frac{\partial}{\partial \phi}(\dot{\phi}\cos\phi F) + \frac{\partial}{\partial \lambda}(\dot{\lambda}F) + \frac{\partial}{\partial \theta}(\dot{\theta}F) = S = S_{\text{in}} + S_{\text{ds}} + S_{\text{nl}} \qquad (1)$$

without restrictions on the shape of the spectrum. Here $F(f, \theta, \phi, \lambda, t)$ denotes the wave energy density as a function of frequency f, direction θ, and time t in a spherical coordinate system (latitude ϕ, longitude λ), $\dot{\phi}$ and $\dot{\lambda}$ denote the components of the group velocity with respect to these coordinates, and $\dot{\theta}$ represents the rate of change of the wave direction θ due to the great circle propagation and (in general, but not considered here) finite depth and current refraction.

The total source function S consists of the sum of the energy input S_{in} due to wind stress forcing [*Snyder et al.*, 1981], the dissipation S_{ds} due to whitecapping [*Komen et al.*, 1984; *K. Hasselmann*, 1974] and (also not considered here) bottom interactions [*K. Hasselmann et al.*, 1973], and the

nonlinear energy transfer S_{nl} [*S. Hasselmann and K. Hasselmann*, 1985; *S. Hasselmann et al.*, 1985].

The wind input source function is taken as

$$S_{in} = \beta F \tag{2}$$

where

$$\beta = \max\left\{0,\ 0.25\ \frac{\rho_a}{\rho_w}\left[28\ \frac{u_*}{c}\cos(\theta - \theta_w) - 1\right]\right\}\omega$$

ρ_a and ρ_w denote the density of air and water, ω is the angular frequency, c is the phase velocity, u^* is the magnitude of the friction velocity $= (\tau/\rho_a)^{1/2}$, where τ denotes the surface stress, and θ_w is the wind direction.

The dissipation of wave energy due to whitecapping is represented as

$$S_{ds} = -2.33 \times 10^{-5}\hat{\omega}\left(\frac{\omega}{\hat{\omega}}\right)^2\left(\frac{\hat{\alpha}}{\hat{\alpha}_{PM}}\right)^2 F \tag{3}$$

where $\hat{\omega}$ is the inverse of the mean period and $\hat{\alpha}$ is an integral wave steepness parameter, which is normalized by the theoretical value $\hat{\alpha}_{PM}$ for a Pierson-Moskowitz spectrum [cf. *S. Hasselmann et al.*, 1988].

The nonlinear transfer is approximated by the discrete interaction parameterization [*S. Hasselmann and K. Hasselmann*, 1985]

$$S_{nl}(\mathbf{k}_4) = \sum_{\gamma=1,2} A_\gamma \omega_4 [n_1^\gamma n_2^\gamma (n_3^\gamma + n_4^\gamma) - n_3^\gamma n_4^\gamma (n_1^\gamma + n_2^\gamma)] \tag{4}$$

where A_γ denotes a (tuned) coupling coefficient and $n_i^\gamma = F_i^\gamma/\omega_i^\gamma$ denotes the action densities at the four wave components $i = 1, \cdots, 4$ of each of the two (mirror-image) discrete resonant interaction quadruplets $\gamma = 1, 2$.

The wind input and the dissipation source function are linear and quasi-linear expressions, respectively, acting only on the spectral wave energy F, whereas the nonlinear interactions couple the different regions of the spectrum. The exact nonlinear transfer function causes the spectral peak of a growing wind sea to shift toward lower frequencies while at the same time preserving the characteristic sharply peaked shape of the developing spectrum [*K. Hasselmann et al.*, 1973]. The discrete interaction approximation, although a strong simplification of the exact expression, reproduces the functional structure and thus the essential peak migration and shape stabilizing features of the full nonlinear transfer function.

For the global Seasat hindcast, the WAM model was run on a 3° × 3° latitude-longitude grid with a directional resolution of 30° and a frequency resolution of 0.1 (25 logarithmically spaced frequencies between 0.04 and 0.45 Hz with $\Delta f/f = 0.1$). The region was bounded at 78°N and 60°S to exclude sea ice areas. The propagation terms were integrated using an upstream scheme with a time step of 40 min, while the source term was integrated implicitly with a time step of 20 min.

Hindcasts were carried out for four different sets of six-hourly global wind or wind stress fields (Table 1). The Goddard Laboratory for Atmospheres fields (1000-hPa winds U_{1000} and surface wind stress fields τ [cf. *Atlas et al.*, 1987]) extended over the entire 96 days of operation of the Seasat scatterometer from July 7 to October 10, 1978. The other two wind data sets covered shorter periods: 2 weeks, September 7–20, for the Jet Propulsion Laboratory 19.5-m-height winds [*Woiceshyn et al.*, 1986] and 10 days, September 6–17, for the European Centre for Medium-Range Weather Forecasts 1000-hPa winds [*Anderson et al.*, 1987].

TABLE 1. Wind Data Sets Used for the Seasat Hindcast

Wind Field	Grid	Latitudinal Coverage	Period
GLA τ	4° × 5°	90° S to 90°N	July 7 to Oct. 10, 1978
GLA U_{1000}	4° × 5°	90° S to 90°N	July 7 to Oct. 10, 1978
JPL $U_{19.5}$	1° × 1°	70° S to 70°N	Sept. 7–20, 1978
ECMWF U_{1000}	1.875° × 1.875°	90° S to 90°N	Sept. 6–17, 1978

All wind fields except JPL were constructed by jointly assimilating conventional meteorological data and Seasat scatterometer winds in an atmospheric model. The GLA 1000-hPa winds U_{1000} were computed using a 4° × 5°, nine-level atmospheric model and an objective analysis scheme. The GLA wind stress fields τ were calculated at each analysis time as the mean over the last 6 hours, using a boundary layer model depending on the atmospheric stability. The ECMWF U_{1000} winds were computed using a more advanced assimilation scheme and a higher-resolution spectral atmospheric model (T63, corresponding to 1.9° × 1.9° resolution, with 19 vertical layers). The JPL 19.5-m winds $U_{19.5}$ were derived by subjective analysis of only the scatterometer winds on a 1° × 1° latitude-longitude grid.

The friction velocities $\mathbf{u}_* = \sqrt{c_D(U)}\mathbf{U}$ needed for the input source function (equation (2)) were derived from the three wind data sets using *Wu*'s [1982] empirical relation

$$\begin{aligned} c_D(U) &= 1.2875 \times 10^{-3} && U < 7.5 \text{ m s}^{-1} \\ c_D(U) &= (0.8 + 0.065U) \times 10^{-3} && U \geq 7.5 \text{ m s}^{-1} \end{aligned} \tag{5}$$

for the drag coefficient c_D, assuming neutral stability. No corrections were introduced to scale the 1000-hPa or 19.5-m winds to the 10-m winds for which Wu's relation was originally derived. This is consistent with the routine application of the WAM model at ECMWF.

Plates 1 and 2 show as example the hindcast fields of monthly mean wave height and propagation direction for August 1978 (the month with the fewest altimeter data gaps), computed using the GLA wind stresses and GLA wind velocities, respectively. The wave heights computed from the stress fields are seen to be systematically lower than the corresponding values for the wind field case, particularly in the high-wind belt in the southern hemisphere.

3. Intercomparison of Hindcast and Altimeter Wave Heights

The Seasat altimeter significant wave height (SWH) data were provided by JPL with an along-track resolution of 7 km (approximately one measurement per second). The orbit repetition period was 17 days from July 7 until September 10, and 3 days for the rest of the Seasat period until October 10. The spacing of successive orbits along the equator was about 2700 km.

To obtain data commensurate with the wave model reso-

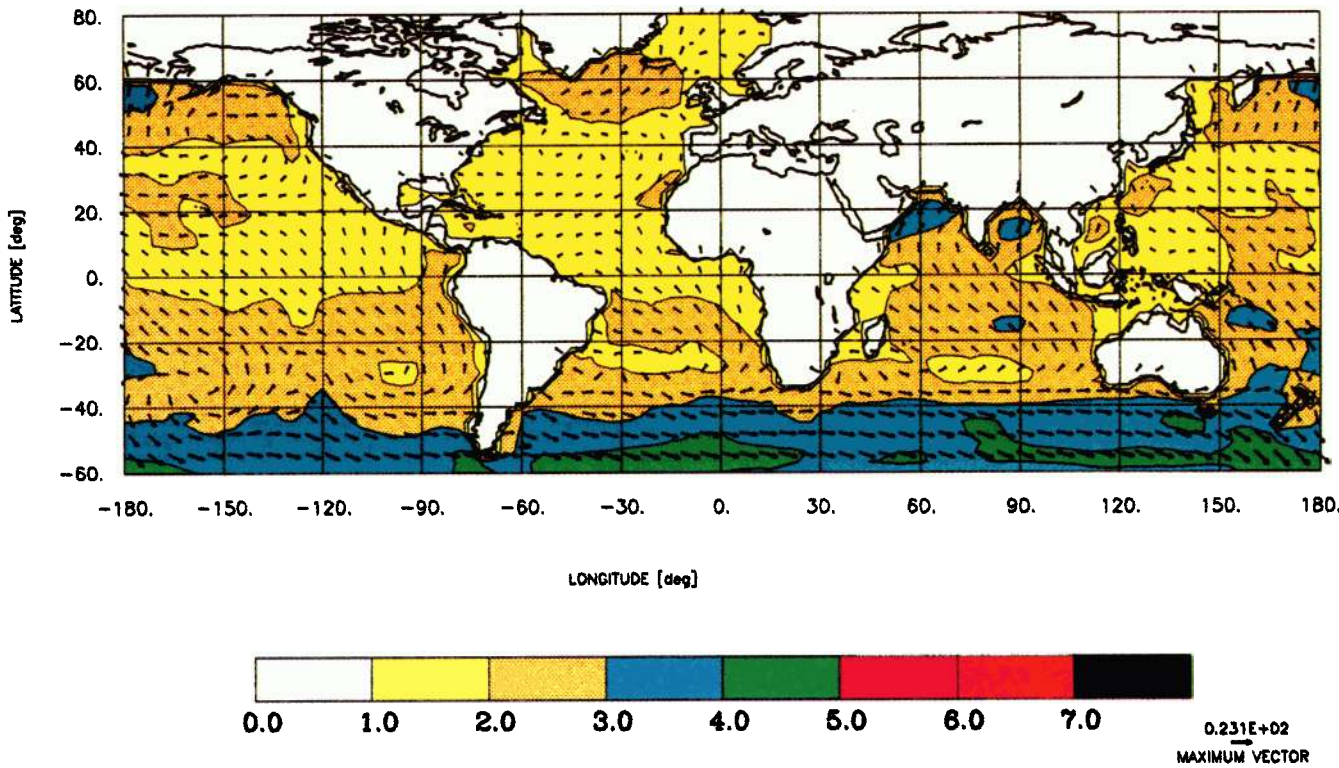

Plate 1. Mean significant wave height and mean direction for the period August 1–28, 1978, derived from the Seasat hindcast using the GLA wind stress fields. Isolines are given in steps of 1 m.

lution, the altimeter time series was smoothed and decimated by averaging over 30-point intervals (≈210 km). In addition, a quality control was carried out, similar to that of *Janssen et al.* [1987], to filter out unrealistic rapid changes in the signal. First, solitary spikes, which often occurred near data gaps, were removed. Spikes were defined as data points which deviated from the mean of an averaging interval by more than twice the standard deviation. After rejection of

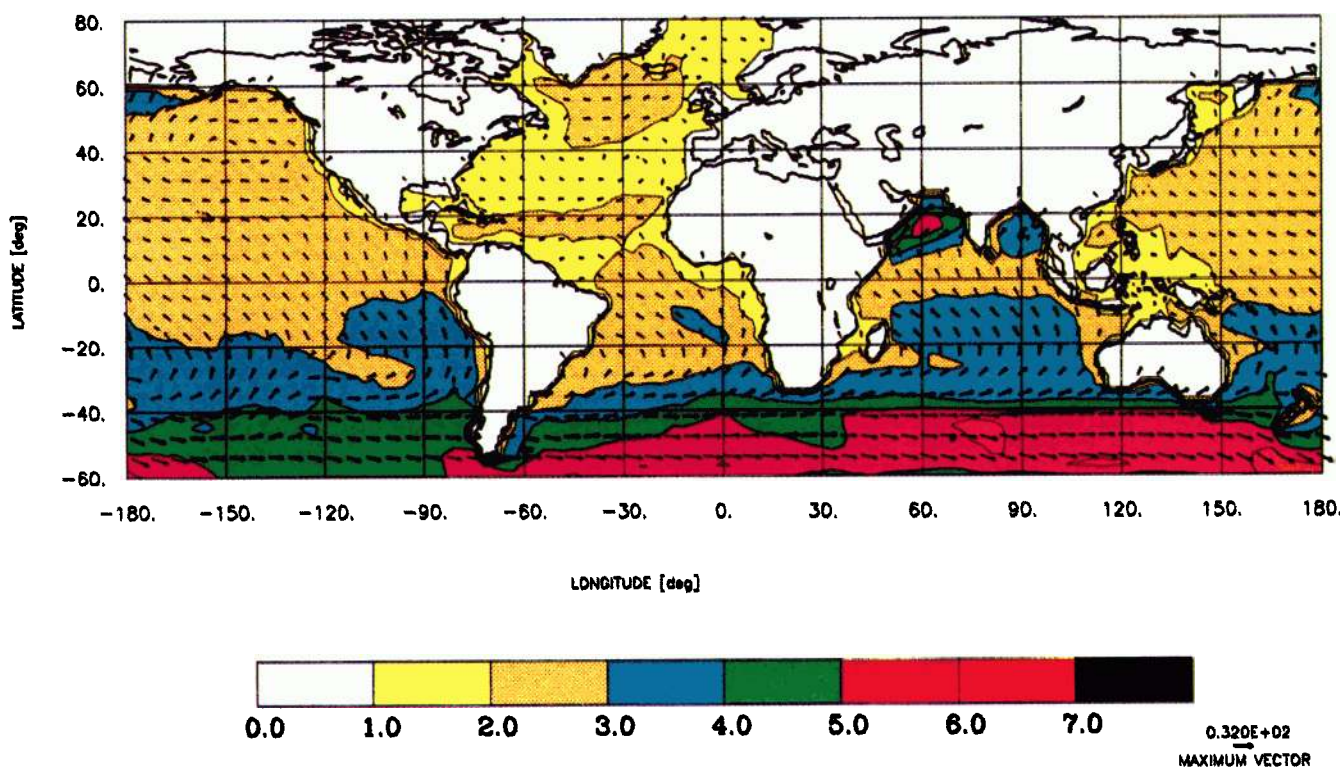

Plate 2. Mean significant wave height and mean direction for the period August 1–28, 1978, derived from the Seasat hindcast using the GLA wind velocity fields. Isolines are given in steps of 1 m.

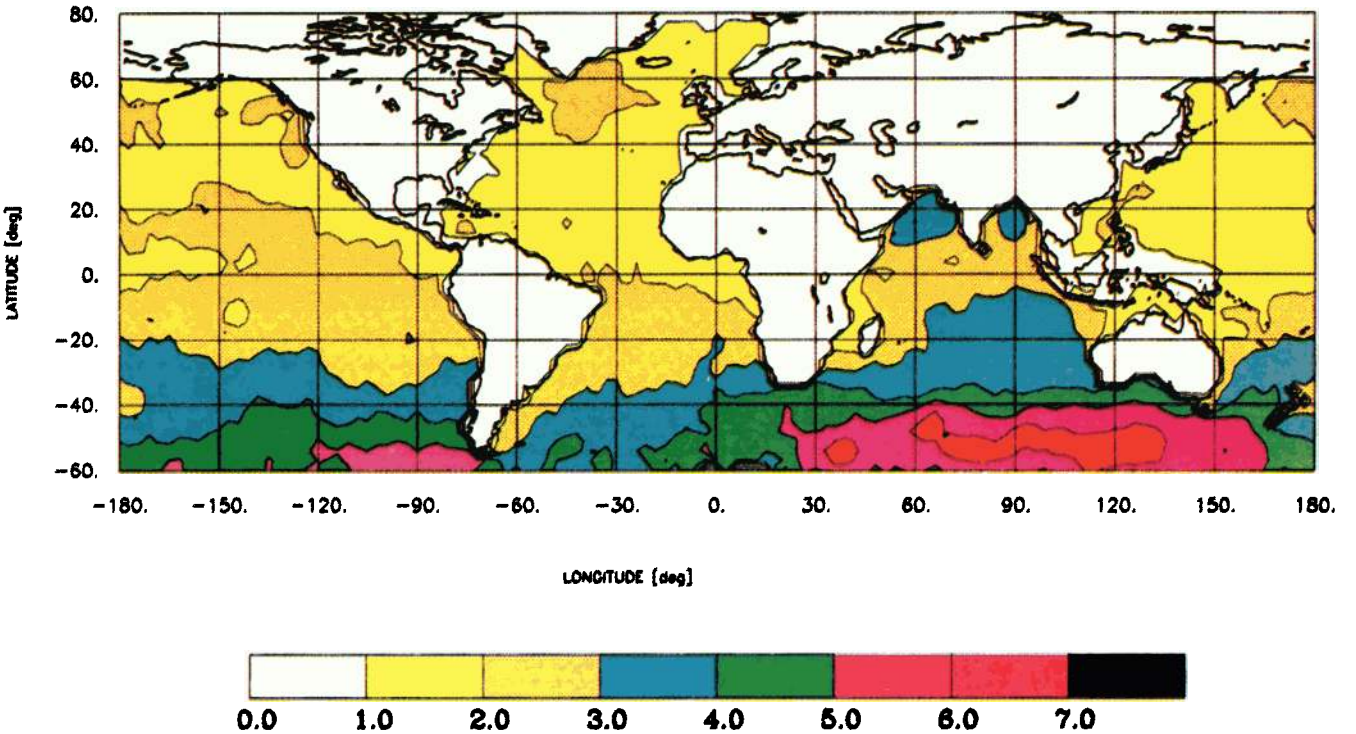

Plate 3. Mean significant wave heights for the period August 1–28, 1978, obtained from the Seasat altimeter observations. Isolines are in steps of 1 m.

spikes, the mean was then recalculated over the residual points of the interval. Intervals consisting of less than 20 residual measurements or with a remaining standard deviation of more than twice the mean were discarded. This led to a rejection of about 7% of the 30-point averages.

Plate 3 shows as example the mean altimeter SWH field for August 1978, which may be compared with the model hindcasts, Plates 1 and 2. The agreement with the hindcast using the GLA stresses (Plate 1) is satisfactory in the northern hemisphere and in the South Atlantic. However, in the high-wind regions of the South Pacific and the Indian Ocean, the model wave heights are lower than the altimeter wave heights by as much as 3 m, or approximately 30–40%. In regions of low wave energy in the tropics, positive and negative deviations of the order of half a meter (25%) are found. In the western tropical Pacific the wave heights are overpredicted. This could be due to shadowing by the Indonesian islands, which cannot be adequately resolved in the wave model.

In contrast to the GLA stress case, the simulated wave heights for the GLA winds agree quite well with the observed wave heights in the strong west wind regions of the southern oceans. However, the wave heights are overestimated in the northern and tropical Pacific, in the monsoon region of the Indian Ocean, and in high latitudes of the southern Atlantic.

To quantify the errors, a statistical intercomparison was carried out on a point-by-point basis for the full period of the hindcasts. For this purpose the 3° × 3° hindcast SWH fields, which were stored every 6 hours, were interpolated onto the positions and times of the 30-point-averaged altimeter time series. Daily averages (indicated by angle brackets) were then formed over the ensembles of colocated data pairs (H_M, H_A) of model and altimeter SWH.

Figures 1 and 2 show the set of daily mean differences (biases) $b = \langle H_M - H_A \rangle$, for the full globe and separately for each hemisphere (2°N to 75°N and 2°S to 60°S), for the two simulations using GLA stress and GLA wind forcing, respectively. Over the 96-day period, the average number of data pairs available per day is 1350, 40% of which are located in the northern hemisphere and 60% in the southern. The large fluctuations on September 6 and 10 are due to the reduction of the number of data pairs on these days to only 440 (10 in the southern ocean) and 115 (69 in the southern ocean), respectively. The globally averaged bias for the GLA stress run is of the order of −0.5 m. Most of this originates in the southern hemisphere. The bias for the northern hemisphere is of the order of only ±0.2 m (except for the dip on September 10; Figure 1). The stablest period is August, which contains the fewest altimeter data gaps. The bias for the hindcast using the GLA winds (Figure 2) is less

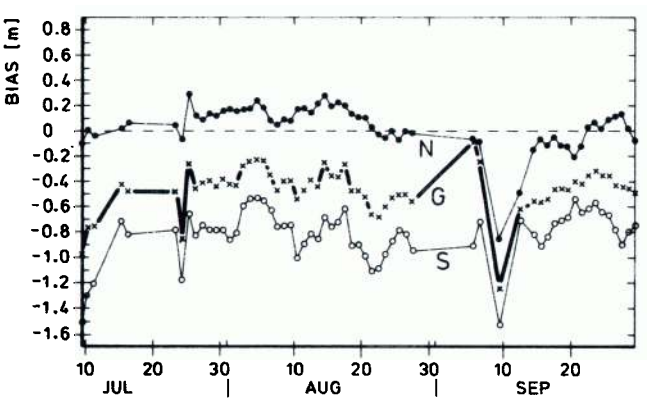

Fig. 1. Daily mean values of the bias of the altimeter SWH relative to the SWH hindcast for the GLA stress case for the period July 10 to October 1. The three graphs represent global (G), northern hemisphere (N), and southern hemisphere (S) data.

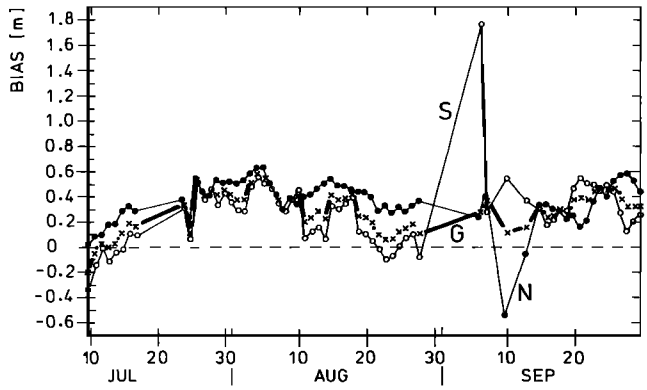

Fig. 2. Same as Figure 1, but for the hindcast using GLA wind velocities.

than that for the GLA stresses and is positive in both hemispheres. The differences between the northern and southern hemispheres in this case are small.

Another statistical quantity of interest is the mean ratio between the observed and modeled wave heights. This can be determined by fitting a regression line

$$y_i = c_y x_i \tag{6}$$

constrained to pass through the origin to the data pairs (x_i, y_i), $i = 1, \cdots, N$, where N is the number of data pairs in a given day. (The standard regression line including an additional additive constant is less useful in the present context, as we are interested primarily in a measure of the mean wave height ratios, not in the optimal linear transformation from one data set to another.)

Minimizing the mean square error $\langle (y - c_y x)^2 \rangle$ in the y direction yields the regression coefficient

$$c_y = \tan \theta_y = \langle xy \rangle / \langle x^2 \rangle \tag{7}$$

Minimization of the mean square error $\langle (x - y/c_x)^2 \rangle$ instead in the x direction yields

$$c_x = \tan \theta_x = \langle y^2 \rangle / \langle xy \rangle \tag{8}$$

From the Cauchy-Schwarz inequality

$$r^2 = \frac{\langle xy \rangle^2}{\langle x^2 \rangle \langle y^2 \rangle} \leq 1 \tag{9}$$

it follows that

$$c_y \leq c_x \tag{10}$$

where the equality sign holds only if all points lie on the regression line.

TABLE 2. Inclination Angles for the Four Different Definitions of a Regression Line Passing Through the Origin as a Function of the Correlation Coefficient r for a Reference Inclination Angle $\theta_y = 47.7°$

Correlation r	θ_y, deg	θ_x, deg	θ, deg	θ', deg
1.0	47.7	47.7	47.7	47.7
0.9	47.7	53.6	50.7	51.4
0.8	47.7	59.8	53.9	56.0
0.7	47.7	65.9	57.5	61.8

A disadvantage of the definitions (7) or (8) is that they are obviously not symmetrical in x and y and in fact have an asymmetrical bias, as expressed by inequality (10). A symmetrical regression coefficient c which is invariant with respect to an interchange of x and y can be defined as

$$c = \tan \theta = (c_x c_y)^{1/2} = (\langle y^2 \rangle / \langle x^2 \rangle)^{1/2} \tag{11}$$

An alternative regression line which has the same interchange symmetry and is invariant moreover with respect to rotations in the xy plane can be defined by minimizing the sum of the orthogonal distances of the data points to the regression line. In this case the regression line is the major axis of the covariance ellipse (defined here with respect to deviations from the origin rather than from the mean), so that

$$c' = \tan \theta' \tag{12a}$$

where

$$\tan 2\theta' = \frac{\langle 2xy \rangle}{\langle x^2 \rangle - \langle y^2 \rangle} \tag{12b}$$

The inclination angles θ and θ' always lie between θ_x and θ_y. The differences between the four regression lines decrease with increasing correlation coefficient r and vanish for $r = 1$, i.e. for vanishing scatter (compare Table 2). In our applications the correlation values are typically of the order of 0.9 or higher, so that the differences between the four definitions are small. We have chosen the symmetrical form c (equation (11)).

Figures 3 and 4 show the computed regression coefficients c for the GLA surface stress and surface wind runs, respectively, as a function of the mean altimeter wave height. The globe has been divided into three (overlapping) regions corresponding to the northern hemisphere (2°N to 75°N), the southern hemisphere (60°S to 2°S), and the tropical region (22°S to 22°N).

The regression coefficients for the wind stress run (Figure 3) scatter around the line $c = 1$ in the northern hemisphere but indicate an underestimation of the model wave heights

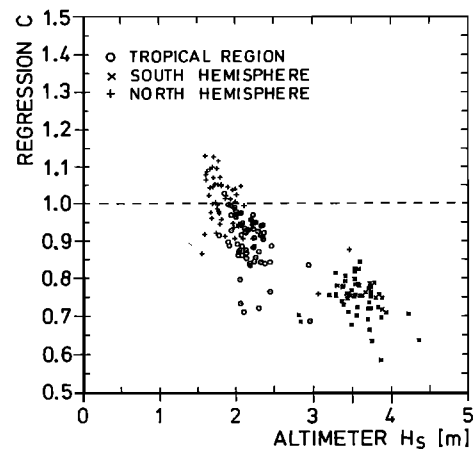

Fig. 3. Regression coefficient c between altimeter and hindcast SWH for the GLA stress forcing case as function of the daily mean altimeter SWH for the period July 10 to October 1. Each point is based on a daily ensemble, where plus signs represent northern hemisphere data; crosses, southern hemisphere data; and circles, tropical data.

relative to the altimeter wave heights by factors between c = 0.6 and 0.85 in the southern hemisphere. The tropical data are bracketed by the two hemispheric data clusters. The results are consistent with the bias data (Figure 1) for August. The regression coefficients for the wind-forcing run (Figure 4) confirm the overestimation of wave energy in the northern hemisphere and in the tropics and indicate a relatively good agreement in the southern hemisphere (compare Figure 2). The correlation coefficients r lie above 0.9 for both hindcast runs.

The predominance of larger wave heights in the southern hemisphere suggests that it may be more appropriate to stratify the differences in the regression coefficients (Figures 3 and 4) with respect to the wave heights rather than geographically. Figures 5 and 6 show the distribution of model wave heights as a function of the altimeter wave heights, independent of the region, for the two GLA simulations (numbers on the standard deviation bars indicate the number of data pairs in each 1-m interval). In both model runs, low significant wave heights are overestimated by the model, while high sea states are strongly underpredicted. The greatest discrepancy is seen for high waves in the GLA stress forcing run: for observed wave heights higher than 8 m, the model underpredicts the wave heights by more than 50% (Figure 5). In the GLA wind-forcing run, on the other hand, satisfactory agreement with the altimeter SWH is found in a relatively wide wave height range from about 2 to 7 m (Figure 6).

To drive the wave model, the GLA winds were converted to stresses using relation (5). Since this does not differ significantly from the boundary layer formulation used in the GLA model, the differences between the hindcasts for the GLA surface stress and surface wind cases must be ascribed to some other numerical, resolution, or sampling problems in the stress calculations. The mutual inconsistency of the GLA stress and wind data was confirmed by a regression analysis in which the square of the GLA wind velocities U_{1000}^2 was related to the square of the GLA friction velocities $u_*^2 = \tau/\rho_a$ (the density of air was taken as ρ_a = 1.23 kg m^{-3}). The regression coefficient c (equation (11)) then defines a spatial mean drag coefficient for each set of wind velocities and stresses at each analysis time:

$$c_D = c = (\langle(\tau/\rho_a)^2\rangle/\langle(U_{1000}^2)^2\rangle)^{1/2} \qquad (13)$$

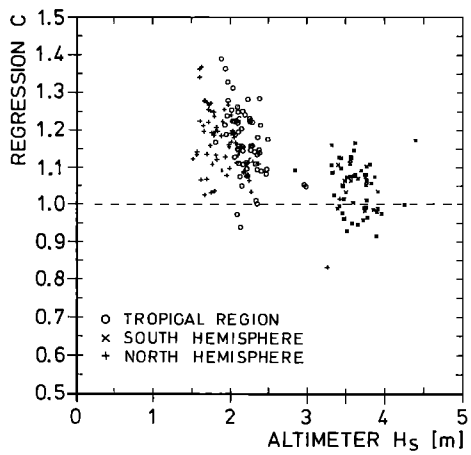

Fig. 4. Same as Figure 3, but for the GLA wind velocity case.

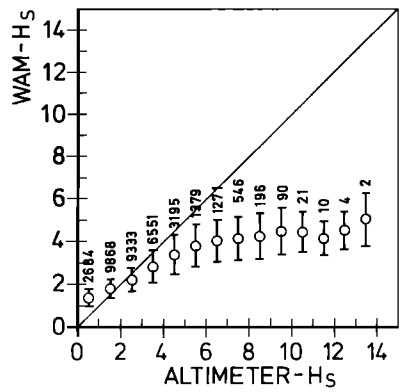

Fig. 5. Mean hindcast wave heights for the GLA friction velocity case versus altimeter wave heights, averaged within 1-m intervals, for the period August 1–31. The number of colocations in each 1-m interval is indicated on the standard deviation error bars.

Figure 7 shows the scatter diagram of c_D for the northern, southern and tropical regions as a function of the associated spatial mean wind speed. The regression coefficients for the northern region are seen to be higher than for the tropical or southern region. The striking decrease of c_D with increasing wind speed contradicts Wu's formula (shown as a solid line) and other empirical and theoretical relations [e.g., *Charnock*, 1955], including the boundary layer formulation used in the GLA model.

A possible explanation of this discrepancy is the difference in the time sampling schemes used to construct the 6-hourly GLA wind and stress fields. The wind fields were determined instantaneously, while the stress fields were computed as time averages over the last 6 hours. Time averaging removes the higher-frequency fluctuations from the stress field, thereby reducing the correlation between the stress field and the instantaneous squared wind field, yielding smaller mean drag coefficients. Since the wave field responds nonlinearly to the stress (for a fully developed wind sea, the wave energy is proportional to the square of the stress), time averaging the stress also reduces the wave model response.

An accurate computation of these effects was not possible, as the high-frequency components filtered out by the averaging procedure were not known. However, estimates based on extrapolating the stress variance spectrum to higher frequencies indicated that time averaging of stress may have contributed substantially to the observed discrepancies.

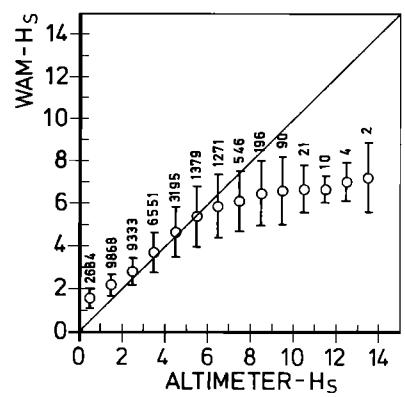

Fig. 6. Same as Figure 5, but for the GLA wind velocity case.

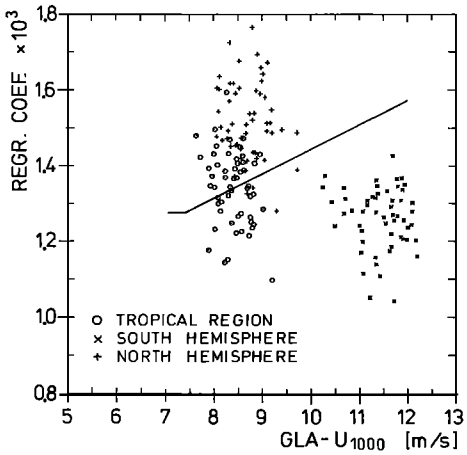

Fig. 7. Regression coefficient c between the GLA wind velocity and the GLA friction velocity as function of the mean wind speed for the period September 6–20. Each point is derived from a regression analysis between two fields at the same instant of time (4 points per day), where plus signs represent northern hemisphere data; crosses, southern hemisphere data; and circles, tropical data. The Wu curve is also shown.

Other contributing factors should nevertheless not be ruled out. Computations of surface stresses in atmospheric general circulation models are notoriously error prone, as the stresses are normally computed as diagnostic variables and have only a weak impact on the evolution of the atmospheric circulation. Inconsistencies have often been discovered only when the atmospheric model was coupled to an ocean model or, as here, to a wave model. Our possible explanation of the discrepancies in the present case is necessarily speculative. The problem cannot be resolved without a more detailed analysis of the atmospheric model (which has since been replaced by an upgraded, higher-resolution version). The main point of the present exercise is to underscore the value of combining the data quality procedures for atmospheric and surface wave data in identifying errors in surface wind or stress fields.

4. Intercomparisons of Hindcast and Altimeter Wave Heights for September 7–17, 1978

In addition to the GLA surface wind and surface stress fields, which were available for the full scatterometer operational period July 7 to October 10, 1978, two other wind fields were available for shorter periods: the subjectively analyzed JPL $U_{19.5}$ winds of *Woiceshyn et al.* [1986] for the period September 7–20 and the model-assimilated ECMWF U_{1000} winds of *Anderson et al.* [1987] for the period September 6–17, 1978. WAM hindcast results were intercompared for the three different global wind velocity fields for the common time period September 7–17 (Table 1).

Although large data gaps existed in the altimeter record during this period, the results obtained with the GLA wind velocities (Figure 8) are compatible with the results obtained for August (Figure 6). The run using the JPL winds (Figure 9) shows, as in the GLA wind case, an overprediction of the low waves by the model and an (even stronger) underprediction of the high waves. The simulated wave heights for the ECMWF winds (Figure 10) are slightly higher than the altimeter wave heights in the entire range from 0 to 11 m. However, the deviations lie within the standard deviation error bounds. *Janssen et al.* [1987] pointed out that the overestimation of the model wave heights on the global average can be attributed to the impact of the assimilated scatterometer winds on the ECMWF wind field analysis: the agreement between model and altimeter wave heights becomes almost perfect when the wave model is driven by the ECMWF conventional wind velocity fields without inclusion of the scatterometer data.

The tendency for the model to overestimate low waves and underestimate high waves may be due to systematic errors in the Seasat-A satellite scatterometer (SASS) algo-

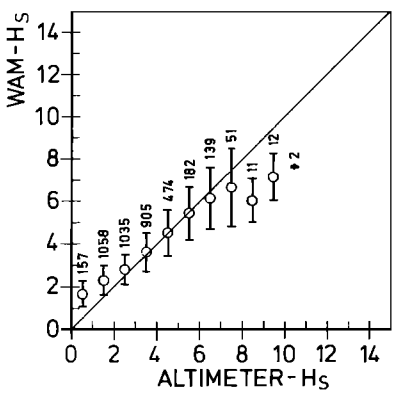

Fig. 8. Mean hindcast wave heights for the GLA wind velocity case versus altimeter wave heights, averaged within 1-m intervals, for the period September 7–17. The number of colocations in each 1-m interval is indicated on the standard deviation error bars.

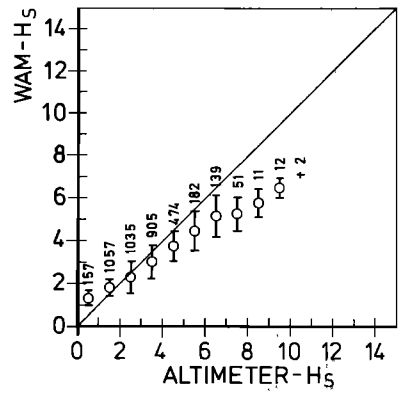

Fig. 9. Same as Figure 8, but for the JPL wind velocity case.

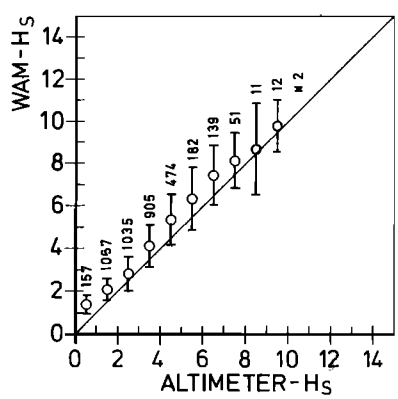

Fig. 10. Same as Figure 8, but for the ECMWF wind velocity case.

TABLE 3. Statistical Intercomparison of 41 Global Wind Velocity Fields From GLA, ECMWF, and JPL for September 7–17, 1978

y Field	x Field	N	$\langle y \rangle$, m s^{-1}	$\langle x \rangle$, m s^{-1}	r	c
GLA	JPL	1540	9.06 ± 0.41	8.46 ± 0.42	0.92	1.09
GLA	ECMWF	1710	9.20 ± 0.39	9.09 ± 0.54	0.93	1.01
ECMWF	JPL	1540	9.00 ± 0.56	8.46 ± 0.42	0.94	1.09

Data are summarized in terms of global mean wind speeds $\langle x \rangle$, $\langle y \rangle$, total root-mean-square deviation (rms), the number of data pairs N for each regression analysis and the mean correlation and regression coefficients r and c, respectively.

rithm [*Wentz et al.* [1986] used to derive the scatterometer winds. *Liu* [1984] and *Anderson et al.* [1987] found that scatterometer winds were systematically higher than ship winds for winds less than about 12 m s^{-1} (which represent the majority of the data), while *Anderson et al.* [1987] found the scatterometer winds to be about 10% too low for high winds between 15 and 25 m s^{-1}.

In order to intercompare the three wind fields, the ECMWF and JPL winds were interpolated onto the coarser 4° × 5° GLA grid. Symmetrized regression coefficients c (equation (11)) were then determined by averaging over all grid points between the latitudes 68°S and 68°N and over all 41 six-hourly global fields during the common period September 7–17. The global mean values obtained for the three pairs of wind data sets are presented in Table 3. The ECMWF and the GLA winds are seen to be reasonably consistent. The JPL winds, however, are low compared with the other two wind data sets (c = 1.09).

Figures 11 and 12 show the scatter diagrams of the globally and hemispherically averaged winds for the set of all 6-hourly wind fields for the wind field pairs GLA-ECMWF and GLA-JPL, respectively. The ECMWF winds agree reasonably well with the GLA winds, although ECMWF winds tend to be lower for low wind speeds and higher for high winds. Possibly this is because the ECMWF winds are provided on a finer grid than the GLA winds and can thus better resolve strong storm events. The JPL winds are lower than the GLA (and therefore also ECMWF) winds by about 10% over the entire wind speed range and in both hemispheres. The correlation coefficients are of the order of 90–95% in all cases.

No significant deviations were found in the wind directions for the three wind fields. For moderate and higher wind speeds the differences in direction were generally less than 20°; larger directional deviations were normally associated with weak winds. More details on the global wind data intercomparison are given by *K. Hasselmann et al.* [1988].

5. Assimilation Experiment

As a first step towards the development of a combined wind and wave data assimilation system, a simple altimeter wave data assimilation experiment was carried out. The assimilation was performed during August 1978 (the month with the fewest data gaps).

The wave data were assimilated into the wave model quasi-continuously at each propagation time step, i.e., every 40 min. This corresponds to the assimilation of an orbit segment of about 17,000 km or eighty 210-km data segments at each assimilation step. The wind field was not changed.

For each observational data point, the model wave spectrum was modified over a finite set of surrounding model grid points by introducing a simple correction factor which varied from a maximum correction at the location of the measurement to unity (no correction) at the edge of the region of influence. Experiments were carried out with different scales L for the region of influence, the scales being chosen such that most of the model grid points received some impact from altimeter wave height measurements within a one day sampling period.

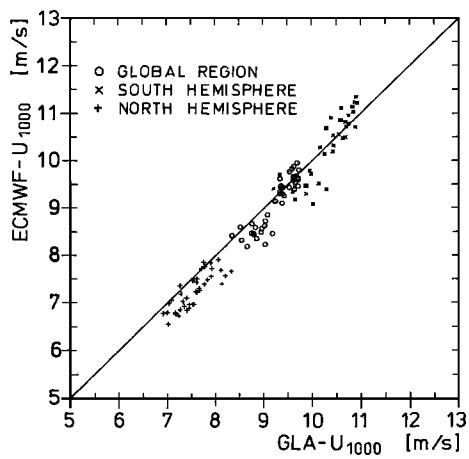

Fig. 11. Mean ECMWF wind speeds for the globe (circles), the northern hemisphere (plus signs), and the southern hemisphere (crosses) as a function of the mean GLA wind speeds for the period September 7–17. Each point represents a spatial mean at an analysis time (four points per day).

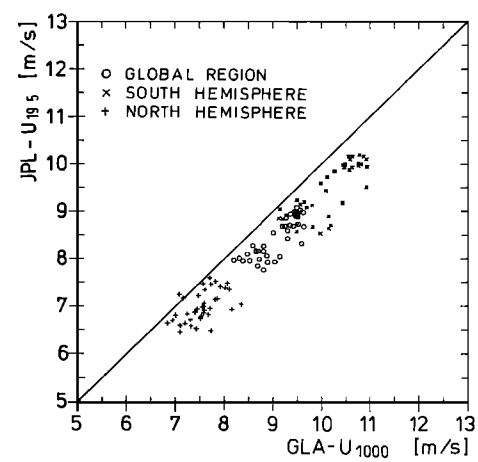

Fig. 12. Mean JPL wind speeds for the globe (circles), the northern hemisphere (plus signs), and the southern hemisphere (crosses) as a function of the mean GLA wind speeds for the period September 7–17. Each point represents a spatial mean at an analysis time (four points per day).

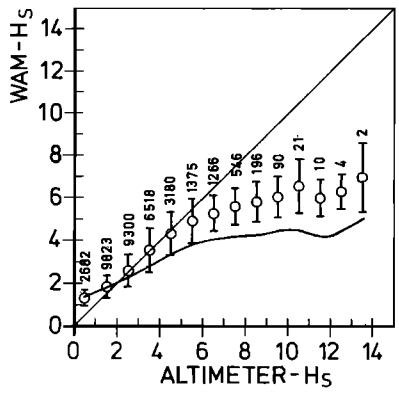

Fig. 13. Mean model wave heights derived from the assimilation experiment with a 15° × 15° region of influence versus altimeter wave heights, averaged within 1-m intervals, for the period August 1–31. The number of colocations in each 1-m interval is indicated on the standard deviation error bars. The solid line shows the distribution before the assimilation (see Figure 5).

The correction factor c_{ij} relating the new spectrum $F_{\text{new}}(f, \theta)$ at a grid point (i, j) to the predicted spectrum $F(f, \theta)$,

$$F_{\text{new}}(f, \theta) = c_{ij}F(f, \theta) \tag{14}$$

was represented as the square of a simple tent (wigwam) function,

$$c_{ij} = \left(1 + w_{ij}\frac{H_A - H_M}{H_M}\right)^2 \tag{15}$$

in which H_A and H_M denote the altimeter and interpolated model wave height at the measurement point, respectively; the weight function is given by

$$\begin{aligned} w_{ij} &= 1 - R \qquad R \le 1 \\ w_{ij} &= 0 \qquad R > 1 \end{aligned} \tag{16}$$

where

$$R = \{0.5[(x_i/L_x)^2 + (y_j/L_y)^2]\}^{1/2} \tag{17}$$

and x_i, y_j represent the distances in the longitude and latitude directions of the model grid point from the measurement point, which are normalized by the corresponding scales L_x, L_y of the region of influence on either side of the measurement point.

Since a given grid point can lie within the region of influence of several altimeter points, the net correction coefficient c_{ij} for a grid point was obtained by forming the average over all correction coefficients collected for the grid point within a propagation (i.e., assimilation) time step.

The application of a constant correction factor to the entire spectrum is the simplest way of adjusting the spectrum to the observed significant wave height. Alternative adjustment prescriptions are conceivable. *Lionello and Janssen* [1990], for example, have recently proposed modifying the wavelength scale of the spectrum simultaneously with the energy scale such that the rms wave slope remains unchanged. The method was motivated by the observation that higher significant wave heights are correlated statistically with longer mean wavelengths, the variations in wave slope being smaller than in either of these two variables separately. Other methods can be applied if independent information is available (e.g., from a SAR) to distinguish wind sea and swell. However, as long as the wind field is not systematically corrected with the aid of the wave model, all such wave spectrum adjustment prescriptions necessarily remain rather arbitrary, and we have therefore simply used the most straightforward technique.

Assimilation experiments were carried out using region-of-influence scales $L_x = L_y = 9°$ (≈900 km) and $L_x = L_y = 15°$ (≈1500 km). As forcing we chose the GLA stress fields, since these yielded the largest deviations from the altimeter data. To remove spin-up effects, the wave model was restarted on July 28 for the August assimilation experiment from the previous July integration.

Figure 13 shows the improvement of the simulated mean wave heights for August achieved in the assimilation run using a 15° region of influence. As expected, the largest improvement is found in regions which are dominated by swell [*K. Hasselmann et al.*, 1988]. Sea states higher than 6 m, which consist mainly of wind sea, are still underpredicted. As the winds were not corrected, the updated wind sea relaxes back rather rapidly in these regions to the original incorrect energy level in response to the erroneous wind forcing. The positive net impact of the wave data assimilation is seen also in Figure 14 which shows the reduction of the global mean SWH bias.

The relaxation time of the assimilation process was investigated in two experiments in which the assimilation process was switched off on August 15, in the middle of the assimilation run. Figure 15 shows the wave height biases for the two switch-off experiments 2 and 3 with 9° and 15° regions of influence, respectively, together with the original uncorrected run 1 already shown in Figure 14. The hindcast relaxes back to the uncorrected bias level within about 5 days in both experiments.

For perfectly updated ocean swell fields, considerably longer relaxation times may have been expected in view of the very weak damping of long ocean swell observed in the Pacific Swell Propagation Study of *Snodgrass et al.* [1966]. However, in the presence of wind sea, the relaxation time is significantly reduced, since the updated wind sea relaxes back rather rapidly, within 1 or 2 days, to the uncorrected windstress forcing.

Another factor reducing the relaxation time is the finite

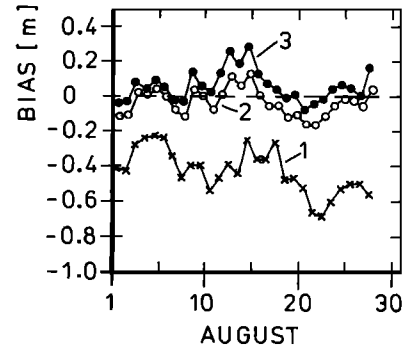

Fig. 14. Daily mean SWH bias for assimilation experiments using the GLA stresses. Curves 2 and 3 represent the bias obtained for 9° and 15° regions of influence, respectively, while curve 1 shows the bias without assimilation.

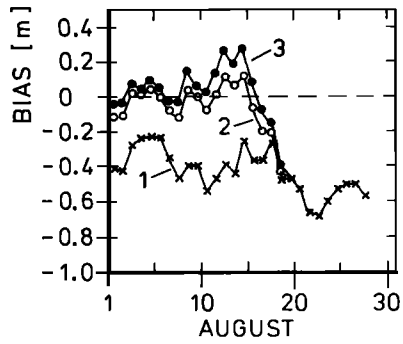

Fig. 15. Same as Figure 14, but with the assimilation switched off on August 15.

spacing of the altimeter tracks. Errors in regions of the ocean which have not been recently updated by altimeter wave height measurements propagate into neighboring updated regions, thereby contaminating the wave field correction. (This was particularly noticeable in a data assimilation exercise by *Janssen et al.* [1989], in which the altimeter information was not distributed over a larger region and the relaxation time was of the order of only 1 day.) An optimal trade-off between a large region of influence desired to cover data gaps and the geophysical limits set by the finite correlation scales of wind fields will clearly be an important consideration in the construction of future more comprehensive wave data assimilation systems.

6. Conclusions

A test of the mutual consistency of Seasat-derived global wind and wave data for the entire Seasat period using a state-of-the-art third-generation wave model yielded valuable insights into the quality of the Seasat altimeter and scatterometer observations. The Seasat exercise is particularly relevant for the ERS satellites, which will carry similar sensors. The study should be viewed as a first step toward the development and implementation of a comprehensive wind and wave data assimilation system for ERS [*K. Hasselmann et al.*, 1988].

The three hindcast experiments using the GLA, ECMWF, and JPL scatterometer-derived wind fields as forcing yielded good general agreement between simulated and observed altimeter wave heights. However, the simulation using the GLA wind stress forcing significantly underpredicted the observed altimeter wave heights in regions of moderate to high wave heights, particularly in the southern ocean. Since the hindcast using the GLA wind field as input yielded satisfactory agreement, and since the WAM model converts input winds into stresses in computing the input source function, we conclude that the origin of the discrepancies must lie in the incompatibility of the GLA surface wind and surface stress fields. This was supported by a direct statistical intercomparison of the two fields. A possible cause of the discrepancy may be the different sampling methods used in constructing the 6-hourly fields: the wind field data represented instantaneous analyzed fields, while the stress fields were computed as 6-hourly averages. We conclude that caution is required in using wind or stress data of low time resolution to drive wave models.

Although significantly smaller, systematic deviations between the simulated and observed altimeter wave heights were found also in the three wind-forcing experiments. In all hindcasts the waves were overpredicted in low sea state regions and underpredicted in high sea state regions. This discrepancy can be attributed in part to systematic errors in the scatterometer algorithm, which tends to overestimate low winds and underestimate high winds. Support for this interpretation is provided by independent intercomparisons of scatterometer and ship winds [*Liu*, 1984; *Anderson et al.*, 1987] and also by the dependence of the errors found in our simulations on the form of wind field analysis. The smallest errors were found in the hindcast using the ECMWF winds, which were derived using a high-resolution (T 63) atmospheric model and a state-of-the-art assimilation scheme based on a large number of conventional observations. The scatterometer data had relatively little impact in this case on the wind field analysis. The largest errors were found for the hindcast using the JPL subjectively analyzed wind fields, which were derived almost exclusively from scatterometer winds.

In an assimilation experiment using the GLA surface stress fields as forcing, altimeter wave height data were continually inserted into the wave model at each 40-min propagation time step over a 1-month period. The corrected wave heights were distributed over a finite region of influence with radius of the order of 1000 km (3–5 grid points) to compensate for the spatial separation of successive satellite orbits. No correction was applied to the wind field. A considerable improvement in the model hindcast was achieved, particularly in regions dominated by swell. The relaxation time of the correction when the assimilation was switched off was of the order of 5 days. We interpret this as an average of the longer relaxation time expected for swell and the considerably shorter relaxation time for wind seas driven by an uncorrected wind field.

Ultimately, more sophisticated assimilation schemes are needed in which the update of the wave field is accompanied by a (nonlocal) update of the wind field. Such techniques are currently being developed [cf. *de Valk and Calkoen*, 1989; K. Hasselmann et al., manuscript in preparation, 1992]. The first attempt presented here to analyze all available Seasat wind scatterometer and altimeter wave height data as a common data set may nevertheless serve to indicate the potential advantages of such an approach for data quality control and future data assimilation applications.

Acknowledgments. The authors are grateful to R. Atlas of the Goddard Laboratory for Atmospheres, P. M. Woiceshyn of the Jet Propulsion Laboratory, and D. Anderson of the European Centre for Medium-Range Weather Forecasts for providing their analyzed global wind fields. This study is a contribution to the research program "Klimarelevante Prozesse im System Ozean-Atmosphäre-Kryosphäre" (SFB 318) funded by the Deutsche Forschungsgemeinschaft and was supported in part by the European Space Agency under study contract 7851/88/HGE-I and the Office of Naval Research under grant N00014-88-J-1025 and 957652 (NSCAT).

References

Alpers, W., Monte Carlo simulations for studying the relationship between ocean wave and synthetic aperture radar image spectra, *J. Geophys. Res.*, *88*, 1745–1759, 1983.

Alpers, W., and C. L. Rufenach, The effect of orbital motions on synthetic aperture radar imagery of ocean waves, *IEEE Trans. Antennas Propag.*, *AP-27*(5), 685–690, 1979.

Anderson, D., A. Hollingsworth, S. Uppala, and P. Woiceshyn, A study of the feasibility of using sea and wind information from the ERS-1 satellite, 1, Wind scatterometer data, ESRIN contract 6297/86/HGE-I(SC), Eur. Cent. for Med. Range Weather Forecasts, Reading, England, 1987.

Atlas, R., A. J. Busalachi, M. Ghil, S. Bloom, and E. Kalnay, Global surface wind and flux fields from model assimilation of Seasat data, *J. Geophys. Res.*, *92*, 6477–6487, 1987.

Brown, R. A., On a satellite scatterometer as an anemometer, *J. Geophys. Res.*, *88*, 1663–1673, 1983.

Brown, R. A., On satellite scatterometer capabilities in air-sea interaction, *J. Geophys. Res.*, *91*, 2221–2232, 1986.

Brüning, C., W. Alpers, L. F. Zambresky, and D. G. Tilley, Validation of a synthetic aperture radar ocean wave imaging theory by the Shuttle Imaging Radar–B Experiment over the North Sea, *J. Geophys. Res.*, *93*, 15,403–15,425, 1988.

Charnock, H., Wind stress on water surface, *Q. J. R. Meteorol. Soc.*, *81*, 639–640, 1955.

Chelton, D. B., and P. J. McCabe, A review of satellite altimeter measurement of sea surface wind speed: With a proposed new algorithm, *J. Geophys. Res.*, *90*, 4707–4720, 1985.

de Valk, C. F., and C. J. Calkoen, Wave data assimilation in a third generation wave prediction model for the North Sea, An optimal control approach, *Rep. H 676*, Delft Hydraul. Lab., Delft, Netherlands, 1989.

Duffy, D., and R. Atlas, The impact of Seasat-A scatterometer data on the numerical prediction of the Queen Elizabeth II storm, *J. Geophys. Res.*, *91*, 2241–2248, 1986.

Fedor, L. A., and G. S. Brown, Wave height and wind speed measurements from Seasat radar altimeter, *J. Geophys. Res.*, *87*, 3254–3260, 1982.

Freilich, M. H., and D. B. Chelton, Wavenumber spectra of Pacific winds measured by Seasat scatterometer, *J. Phys. Oceanogr.*, *16*, 741–757, 1986.

Hasselmann, K., On the spectral dissipation of ocean waves due to white capping, *Boundary Layer Meteorol.*, *6*, 107–127, 1974.

Hasselmann, K., Assimilation of microwave data in atmospheric and wave models in the use of satellite data in climate models, *Eur. Space Agency Spec. Publ., ESA-SP 244*, 47–52, 1985.

Hasselmann, K., and S. Hasselmann, On the nonlinear mapping of an ocean wave spectrum into a synthetic aperture radar image spectrum and its inversion, *J. Geophys. Res.*, *96*, 10,713–10,729, 1991.

Hasselmann, K., et al., Measurements of wind-wave growth and swell decay during the Joint North Sea Wave Project (JONSWAP), Ergänzungsheft zur *Dtsch. Hydrogr. Z.*, *8*(12), suppl. A, 95 pp., 1973.

Hasselmann, K., R. K. Raney, W. J. Plant, W. Alpers, R. A. Shuchman, D. R. Lyzenga, C. L. Rufenach, and M. J. Tucker, Theory of synthetic aperture radar ocean imaging: A MARSEN view. *J. Geophys. Res.*, *90*, 4659–4686, 1985.

Hasselmann, K., S. Hasselmann, E. Bauer, C. Brüning, S. Lehner, H. Graber, and P. Lionello, Development of a satellite SAR image spectra and altimeter wave height data assimilation system for ERS-1, final report, ESA study contract 6875/87/HGE-I(SC), *Rep. 19*, 155 pp., Max-Planck-Inst. für Meteorol., Hamburg, Germany, 1988.

Hasselmann, K., S. Hasselmann, C. Brüning, and A. Speidel, Interpretation and application of SAR wave image spectra in wave models, in *Directional Ocean Wave Spectra*, edited by R. C. Beal, pp. 117–124, Johns Hopkins University Press, Baltimore, Md., 1991.

Hasselmann, S., and K. Hasselmann, Computations and parameterizations of the nonlinear energy transfer in a gravity wave spectrum, I, A new method for efficient computation of the exact nonlinear transfer integral, *J. Phys. Oceanogr.*, *15*, 1369–1377, 1985.

Hasselmann, S., K. Hasselmann, J. H. Allender, and T. P. Barnett, Computations and parameterizations of the nonlinear energy transfer in a gravity wave spectrum, II, Parameterizations of the nonlinear energy transfer for application in wave models, *J. Phys. Oceanogr.*, *15*, 1378–1391, 1985.

Hasselmann, S., et al. (WAMDI Group), The WAM model—A third generation ocean wave prediction model, *J. Phys. Oceanogr.*, *18*, 1775–1810, 1988.

Hoffman, R. N., SASS wind ambiguity removal by direct minimization, *Mon. Weather Rev.*, *110*, 434–445, 1982.

Hoffman, R. N., SASS wind ambiguity removal by direct minimization, II, Use of smoothness and dynamical constraints, *Mon. Weather Rev.*, *112*, 1829–1852, 1984.

Janssen, P. A. E. M., P. Lionello, M. Reistad, and A. Hollingsworth, A study of the feasibility of using sea and wind information from ERS-1 satellite, 2, Use of scatterometer and altimeter data in wave modelling and assimilation, ESRIN contract 6297/86/HGE-I(SC), Eur. Cent. for Med. Range Weather Forecasts, Reading, England, 1987.

Janssen, P. A. E. M., P. Lionello, M. Reistad, and A. Hollingsworth, Hindcasts and data assimilation studies with the WAM model during the Seasat period, *J. Geophys. Res.*, *94*, 973–993, 1989.

Komen, G. J., S. Hasselmann, and K. Hasselmann, On the existence of a fully developed windsea spectrum, *J. Phys. Oceanogr.*, *14*, 1271–1285, 1984.

Lionello, P., and P. A. E. M. Janssen, Assimilation of altimeter measurements to update swell spectra in a wave model, paper presented at International Symposium on Assimilation of Observations in Meteorology and Oceanography, Am. Meteorol. Soc., Clermont-Ferrand, France, July 9–13, 1990.

Liu, W. T., The effects of the variations in sea surface temperature and atmospheric stability in the estimation of average wind speed by Seasat-SASS, *J. Phys. Oceanogr.*, *14*, 392–401, 1984.

Mognard, N. M., W. J. Campbell, R. E. Cheney, J. G. Marsh, and D. B. Ross, Southern ocean waves and winds derived from Seasat altimeter measurements, in *Wave Dynamics and Radio Probing of the Ocean Surface*, edited by O. M. Phillips and K. Hasselmann, pp. 479–489, Plenum, New York, 1986.

Pierson, W. J., Jr., and L. Moskowitz, A proposed spectral form for fully developed wind seas based on the similarity theory of S. A. Kitaigorodskii, *J. Geophys. Res.*, *69*, 5181–5203, 1964.

Queffeulou, P., Seasat wave height measurements: A comparison with sea truth data and a wave forecasting model—Application to the geographic distribution of strong sea states in storms, *J. Geophys. Res.*, *88*, 1779–1788, 1983.

Romeiser, R., Vergleich von berechneten Wellenhöhen des WAM-Seegangsmodells mit gemessenen Daten des Geosat-Satelliten, diplomarbeit, Univ. Bremen, Bremen, Germany, 1990.

Snodgrass, F. E., G. W. Groves, K. F. Hasselmann, G. R. Miller, W. H. Munk, and W. H. Powers, Propagation of ocean swell across the Pacific, *Philos. Trans. R. Soc. London, Ser. A*, *259*, 431–497, 1966.

Snyder, R. L., F. W. Dobson, J. A. Elliott, and R. B. Long, Array measurements of atmospheric pressure fluctuations above surface gravity waves, *J. Fluid Mech.*, *102*, 1–59, 1981.

Schroeder, L. C., D. H. Boggs, G. Dome, I. M. Halberstam, W. L. Jones, W. J. Pierson, and F. J. Wentz, The relationship between wind vector and normalized radar cross section used to derive Seasat-A satellite scatterometer winds, *J. Geophys. Res.*, *87*, 3318–3336, 1987.

Thomas, J., Retrieval of energy spectra from measured data for assimilation into a wave model, *Q. J. R. Meteorol. Soc.*, *114*, 781–800, 1988.

Wentz, F. J., L. A. Mattox, and S. Peteherych, New algorithms for microwave measurements of ocean winds: Applications to Seasat and the special sensor microwave imager, *J. Geophys. Res.*, *91*, 2289–2307, 1986.

Woiceshyn, P. M., M. G. Wurtele, D. H. Boggs, L. F. McGoldrick, and S. Peteherych, The necessity for a new parameterization of an empirical model for wind/ocean scatterometry, *J. Geophys. Res.*, *91*, 2273–2288, 1986.

Wu, J., Wind-stress coefficients over sea surface from breeze to hurricane, *J. Geophys. Res.*, *87*, 9704–9706, 1982.

E. Bauer, Institut für Meereskunde, Universität Hamburg, Troplowitzstrasse 7, D-2000 Hamburg 54, Germany.

H. C. Graber, Applied Marine Physics, RSMAS, University of Miami, 4600 Rickenbacker Causeway, Miami, FL 33149-1098.

K. Hasselmann and S. Hasselmann, Max-Planck-Institut für Meteorologie, Bundesstrasse 55, D-2000 Hamburg 13, Germany.

(Received July 18, 1991;
revised February 21, 1992;
accepted February 24, 1992.)